

Model-Based Single Image Deep Dehazing

Zhengguo Li
I²R A-STAR

Chaobing Zheng
WUST*

Haiyan Shu
I²R A-STAR

Shiqian Wu
WUST

Abstract

Model-based single image dehazing algorithms restore images with sharp edges and rich details at the expense of low PSNR values. Data-driven ones restore images with high PSNR values but with low contrast, and even some remaining haze. In this paper, a novel single image dehazing algorithm is introduced by fusing model-based and data-driven approaches. Both transmission map and atmospheric light are initialized by the model-based methods, and refined by deep learning approaches which form a neural augmentation. Haze-free images are restored by using the transmission map and atmospheric light. Experimental results indicate that the proposed algorithm can remove haze well from real-world and synthetic hazy images.

1. Introduction

Visual signals are distorted in adverse weather conditions which are usually classified as steady (such as haze, mist, and fog) or dynamic (such as rain and snow) [1, 2]. The haze issue is studied in this paper. Due to the effect of light scattering through small particles accumulated in the air, hazy images suffer from contrast loss of captured objects [1], color distortion [3, 4], and reduction of dynamic range [5, 6]. Existing object detection algorithms might not perform well on the hazy images, especially for those real-world hazy images with heavy haze. Haze is also an issue for heavy rain images [2]. It is thus important to study single image dehazing for both hazy and rainy images.

Single image dehazing is widely studied because of its broad applications. Two popular types of single image dehazing algorithms are model-based ones [4, 7, 8, 9, 10] and data-driven ones [11, 12, 13, 16, 14, 15]. The model-based ones are on top of the Koschmieders law [17]. They can improve the visibility of real-world hazy images well regardless of haze degree but they cannot achieve high PSNR and SSIM values on the synthetic sets of hazy images. On the other hand, the data-driven ones perform well on the synthetic sets while their performance is poor for real-world hazy images, especially for those hazy images with heavy haze [18, 19]. It is thus desired to have a single image de-

hazing algorithm which is applicable for both the synthesized and the real-world hazy images.

In this paper, a novel single image dehazing algorithm is proposed by fusing the model-based and data-driven approaches. Same as the model-based methods in [4, 7, 8, 9, 10] and the data-driven ones such as [12], both the atmospheric light and the transmission map are required by the proposed algorithm. Rather than using the model-based methods in [4, 8, 9, 10] or the data-driven methods in [12, 20], they are initialized by using model-based methods, and refined by data-driven approaches. The atmospheric light is initialized by using the hierarchical searching method in [21] which is based on the Koschmieders law [17]. The transmission map is initialized by using the dark direct attenuation prior (DDAP) in [10] which is extended from the dark channel prior (DCP) in [4]. The DDAP is applicable to all the pixels in the hazy image. Unfortunately, the initial transmission map suffers from morphological artifacts. The morphological artifacts caused by the DDAP are then reduced by the novel haze line averaging algorithm in [10] which is designed by using the concept of haze line in [9].

The initial atmospheric light and transmission map are then refined via data-driven approaches. Pre-trained deep neural networks (DNNs) can be served as fast solvers for complex optimization problems [25, 33]. Such an advantage of data-driven approaches is well utilized by our refinement. Since it is very difficult or even impossible to have a pair of a real-world hazy image and its corresponding haze-free image, the popular generative adversarial network (GAN) [38] is utilized to refine the atmospheric light and transmission map. The initial atmospheric light and transmission map can be regarded as noisy atmospheric light and transmission map. The main function of the GAN is to reduce the noise of the initial atmospheric light and transmission map. Based on this observation, the generator of the proposed GAN is constructed on top of the latest DNN for noise reduction in [22] and the Res2Net in [23]. The discriminator of the proposed GAN is based on the PatchGAN in [24].

The proposed GAN is trained by using 500 hazy images from the multiple real-world foggy image defogging (MR-

*Correspondence author

FID) dataset in [19] and 500 hazy images from the realistic single image dehazing (RESIDE) dataset in [40]. The hazy images in the RESIDE dataset are synthesized by using the Koschmieders law [17]. Existing data-driven dehazing algorithms such as [14, 15, 31, 39] are trained by using more than 10K hazy images in the RESIDE dataset in [40]. All ground-truth images of haze-free images in the RESIDE dataset [40] are available. The l_1 loss function can be applied to measure the restored images for those hazy images in the RESIDE dataset. There is a clean image for each hazy image in the MRFID dataset but the clean and hazy images are captured under different lighting conditions. A new loss function is derived by using an extreme channel which is extended from the dark channel in [4]. The new loss function, the adversarial loss function [38], and one more loss function on the gradient of the restored image are used to measure the restored images for the hazy images in the MRFID dataset. The proposed GAN is trained by integrating the l_1 loss function for all images in the RESIDE dataset and the three loss functions for all images in the MRFID dataset in each batch. They are analogous to the data-fidelity term and the regularization term of the optimization problems in [26, 37], respectively.

The model-based estimation and the data-driven refinement forms a neural augmentation which can be applied to improve the interpretability of pure data-driven approaches [25]. Experimental results show that the proposed algorithm is applicable to the synthetic and real-world hazy images, and outperforms existing data-driven dehazing algorithms for the real-world hazy images from the dehazing quality index (DHQI) point of view [41]. One contribution is to propose a novel model-based deep learning framework which fuses model-based and data-driven approaches for single image dehazing. The framework is applicable to the synthetic and real-world hazy images. The number of training data can be reduced significantly. The second contribution is to propose selection of suitable loss functions according to the lighting conditions of the hazy and clean images. Different loss functions are utilized to measure the hazy images in the RESIDE and MRFID datasets.

The remainder of this paper is organized as below. Relevant works on single image dehazing are summarized in Section 2. Details of the proposed algorithm are presented in Section 3. Experimental results are provided to verify the proposed algorithm in Section 4. Finally, conclusion remarks are provided in Section 5.

2. Related Works

Suppose that Z is a hazy image and I is the corresponding haze-free image. The relationship between them can be represented by the following Koschmieders law [17]:

$$Z_c(p) = I_c(p)t(p) + A_c(1 - t(p)), \quad (1)$$

where $p(= (i, j))$ is a pixel position, and $c \in \{R, G, B\}$ is a color channel. A_c is the atmospheric light, and t is the transmission map. When the atmosphere is homogenous, $t(p)$ can be computed by $\exp^{-\alpha d(p)}$, in which $\alpha(> 0)$ represents the scattering coefficient of the atmosphere. $d(p)$ is the depth of pixel (p) . The term $I_c(p)t_c(p)$ is called direct attenuation, and the term $A_c(1 - t(p))$ is called airlight.

By using the equation (1), both visibility and color saturation of a hazy image are reduced. On the other hand, under-exposed and over-exposed regions of the image I could become well-exposed ones in the hazy image Z due to the airlight, and the dynamic range of Z is reduced [?, 5]. Generally, the visual quality of a hazy image becomes poor if the haze is heavy [26]. It is thus important to restore the haze-free image I . Single image dehazing is a challenging problem because the transmission map t depends on the unknown and varying depth. There are two popular types of algorithms: model-based and data-driven ones.

Many model-based dehazing algorithms were proposed by using the model (1). Both the atmospheric light and the transmission map have to be estimated by the model-based methods. Since the number of freedoms is larger than the number of observations, single image dehazing is an ill-posed problem. Different priors were proposed to reduce the number of freedoms [4, 7, 8, 9]. Among them, the well known DCP in [4] assumes that each local patch of an outdoor haze-free image includes at least one pixel which has at least one color channel with a small intensity. The DCP introduces morphological artifacts to the restored image. Guided image filter (GIF) [35] and weighted GIF (WGIF) [36] can be selected to reduce the morphological artifacts. A color-line prior was proposed in [7] by using an observation that small image patches typically exhibit a 1D distribution in the RGB color space. The haze line prior (HLP) in [9] is based on an observation that the a finite number of different colors which are classified into clusters can represent colors of a haze-free image in the RGB space [34]. All the corresponding pixels in each cluster form a haze line in the hazy image. The HLP assumes that there exist at least one haze-free pixel in each haze line. The artifacts of the transmission map caused by the HLP are reduced by using the weighted least squares (WLS) framework [37].

The priors in [4, 9] are robust to haze degree in hazy images. Unfortunately, both the DCP in [4] and the HLP in [9] are not true for those pixels in the sky region. A new DDAP was extended from the DCP such that the prior is applied for all the pixels in a hazy image [10]. In addition, these physical priors are not always reliable, leading to inaccurate transmission estimates and producing artifacts in the restored images. The concept of haze line in [9] was adopted in [10] to form a haze line averaging algorithm which can reduce the morphological artifacts caused by the DCP and DDAP significantly. The transmission map is usually re-

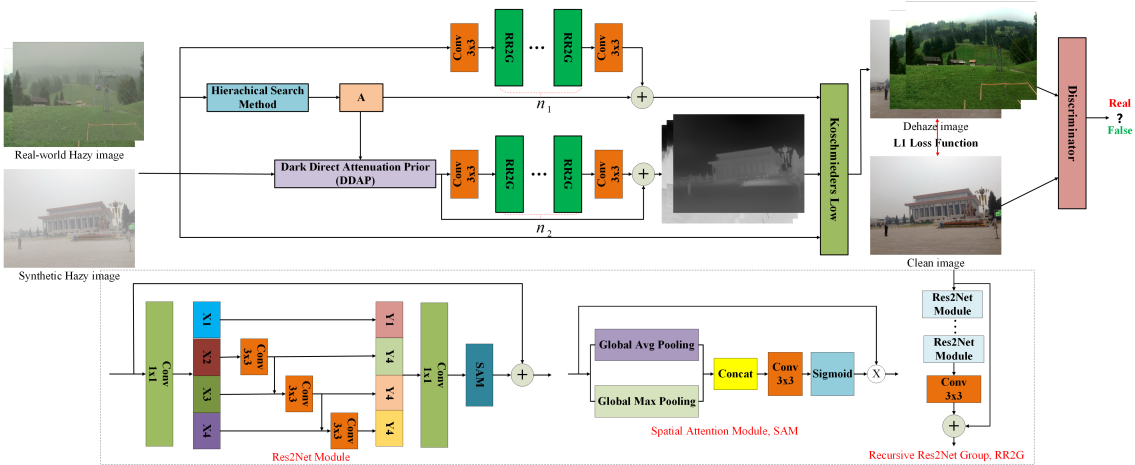


Figure 1. The proposed framework for single image dehazing via model-based GAN. The generator is on top of the DNN in [22], and the discriminator is based on the PatchGAN in [24]. Each dual attention block (DAB) [22] contains spatial attention and channel attention modules. The Recursive Residual Group (RRG) contains several DABs and one 3×3 convolution layers.

fined by solving a complex optimization problem [4, 9]. Fortunately, the optimal solution can be approximated by a pre-trained DNN [25]. Amplification of noise in the sky region could also be an issue for the model-based dehazing algorithms [18, 26].

There are many data-driven dehazing algorithms, especially deep learning based dehazing algorithms. Convolutional neural networks (CNNs) based algorithms such as [11, 12, 14, 15] have potential to obtain higher SSIM or PSNR values but the dehazed images look blurry and they are not photo realistic. Their performance is poor if the haze is heavy [18]. Qu et al. [16] proposed an interesting GAN based dehazing algorithm on top of the physical scattering model [17]. Dong et al. [39] proposed a fully end-to-end GAN with fusion discriminator (FD-GAN) which takes frequency information as additional priors for single image dehazing. The GAN based dehazing algorithm is able to produce photo-realistic images even though generated texture and real one could be different. This problem could be addressed by using the hazy image dataset in [19] to train the GANs. Large pairs of hazy and clean images are necessary for the training of the data-driven methods. Most data-driven methods are trained on synthetic hazy images [27, 28]. Due to the domain gap between synthetic and real-world data, recent investigations indicate that the data-driven algorithms perform well for synthesized hazy images but poor for real-world hazy images [18, 19]. This is because that it is almost impossible to obtain the ground-true depth information in most real-world scenarios. The DCP and GANs were used [29, 30, 31] to address the problem of lacking paired training images for real-world hazy images.

The model-based dehazing algorithms can remove haze regardless of haze degree but they could introduce artifacts duo to the inaccurate estimation of A and t . On the other

hand, the data-driven ones produce visually pleasing results but they do not perform well for real-world hazy images, especially for those images with heavy haze. In this paper, the model-based and data-driven dehazing algorithms are fused together to develop a neural augmented single image dehazing framework. In such a framework, the model-based dehazing algorithm is helpful to reduce the complexity of the data-driven one. The DCP [4] was also applied to estimate the transmission map and atmospheric light in the RefinedNet [31]. Only the transmission map is refined by a data-driven approach in [31] while both the atmospheric light and the transmission map are refined by using data-driven approaches in the proposed algorithm. The GIF [35] was used in [31] to reduce the morphological artifacts caused by the DCP while the simple haze line averaging algorithm in [10] is used in the proposed algorithm. As pointed out in [32], the simplicity of the model-based method is very important for the neural augmentation. A perceptual fusion strategy is also adopted in the RefinedNet to blend two different dehazing outputs which further increases the complexity of the RefinedNet. In addition, the RefinedNet is trained by using 13,990 synthetic hazy images in the RE-SIDE dataset [40] while the proposed framework is trained by only using 1000 hazy images.

3. Neural Augmented Single Image Dehazing

Same as the algorithms in [4, 8, 9, 10], both the atmospheric light A and the transmission map t are required by the proposed algorithm to restore the haze-free image I . They are initialized by model-based methods, and refined by data-driven approaches. The model-based and data-driven approaches form a neural augmentation [25]. The overall framework is shown in Figure 1, and it is very neat.

The proposed framework well utilizes the approximation capability of multi-layer neural networks [33].

3.1. Model-Based Initialization of A and t

3.1.1 Initialization of A

It can be derived from the model (1) that the transmission map $t(p)$ is almost zero and the value of $Z_c(p)$ is A_c for a pixel p in the sky region. Thus, the variance of pixel values is usually very small and the average of pixel values is usually large in the sky region. Based on this observation, a novel hierarchical searching method was proposed in [21] to estimate the atmospheric light A . The method is also adopted by the proposed framework to estimate an initial value of the atmospheric light A . The hazy image Z is divided into four rectangular regions. The score of each region is defined as the mean of the average pixel value subtracted by the standard deviation of the pixel values within the region along all the color channels. The region with the highest score is further divided into four smaller regions. This process is repeated until the size of the selected region is smaller than a pre-specified threshold such as 32×32 . Within the finally selected region, the color vector, which minimizes the distance $\|[Z_r(p) - 255, Z_g(p) - 255, Z_b(p) - 255]\|$ is selected as the atmospheric light. The initial A might not be very accurate, it will be refined by using a data-driven approach.

3.1.2 Initialization of t

The transmission map t is first estimated by using the DDAP in [10] which is applicable to all pixels in the hazy image Z . The dark direct attenuation of a hazy image Z is defined as [10]

$$\psi_\rho(I * t)(p) = \min_{p' \in \Omega_\rho(p)} \left\{ \min_{c \in \{R, G, B\}} \{I_c(p') t(p')\} \right\}, \quad (2)$$

where $\Omega_\rho(p)$ is a square window centered at the pixel p of a radius ρ which is usually selected as 7.

The DDAP assumes that $\psi_\rho(I * t)(p)$ is zero for the pixel p . An initial transmission map $t_0(p)$ is estimated by using the DDAP as

$$t_0(p) = 1 - \psi_\rho\left(\frac{Z}{A}\right)(p). \quad (3)$$

For any pixel p , it can be derived from the equations (1) and (3) that

$$\frac{t_0(p)}{\|Z(p) - A\|} = \frac{1}{\|I(p) - A\|}. \quad (4)$$

However, the operation in (2) could introduce morphological artifacts. Therefore, the equation (4) becomes

$$\frac{t_0(p)}{\|Z(p) - A\|} = \frac{1}{\|I(p) - A\|} + e(p), \quad (5)$$

where $e(p)$ is the morphological artifact caused by the DDAP.

As shown in Figure 2(c), there are indeed visibly morphological artifacts in the restored image I if the $t_0(p)$ is directly applied to remove the haze from the hazy image Z . The haze line averaging method in [10] is adopted to reduce the morphological artifacts. The haze line averaging is on top of the following haze line $H(p'')$ [9]:

$$H(p'') = \{p \mid \sum_{c \in \{R, G, B\}} |I_c(p'') - I_c(p)| = 0\}. \quad (6)$$

Each haze line can be identified by using a color shift hazy pixel which is defined as $(Z(p) - A)$. The $(Z(p) - A)$ can be converted into the spherical coordinates, $[r(p), \theta(p), \psi(p)]$ where $\theta(p)$ and $\psi(p)$ are the longitude and latitude, respectively, and $r(p)$ is $\|Z(p) - A\|$.

The morphological artifacts in the equation (5) can be reduced by the following haze line averaging [10]:

$$t(p) = \frac{\sum_{p' \in H_s(p'')} t_0(p')}{\sum_{p' \in H_s(p'')} r(p')} r(p), \quad (7)$$

where $H_s(p'')$ is a subset of $H(p'')$, and it is obtained as follows:

A 2-D histogram binning of θ and ψ with uniform edges in the range $[0, 2\pi] \times [0, \pi]$ is adopted to generate an initial set of $H(p'')$. The bin size is chosen as $\pi/720 \times \pi/720$. An upper bound ν is defined for the cardinality of the final sets. It is usually selected as 200. Let $|H(p'')|$ be the cardinality of the set $H(p'')$. The set $H(p'')$ is dividedly into $\max\{1, |H(p'')|/\nu\}$ sub-sets for a non-empty $H(p'')$.

The haze-line averaging (7) integrates the DDAP and the concept of haze line in [9] seamlessly. As illustrated in Figure 2(d), the morphological artifacts are significantly reduced by the haze-line averaging (7). On the other hand, there is remaining artifacts and it will be removed by a data-driven refinement.

3.2. Data-Driven Refinement of A and t

3.2.1 Structure of Data-Driven Refinement

Instead of using the GIF [35] or the WGIF [36], a DNN is served to refine the transmission map t in the equation (7) in this subsection. The atmospheric light A is also refined by a DNN as shown in Figure 1. The DNN for the atmospheric light is simpler than the DNN for the transmission map.

It is very difficult or even impossible to obtain the corresponding haze-free image I for a real-world hazy image Z . Thus, the GAN [38] is utilized to refine the atmospheric light and transmission map. As indicated in the introduction, the initial transmission map and atmospheric light are noisy. The generator is thus built up on top of the latest DNN for the noise reduction in [22]. The residual net in

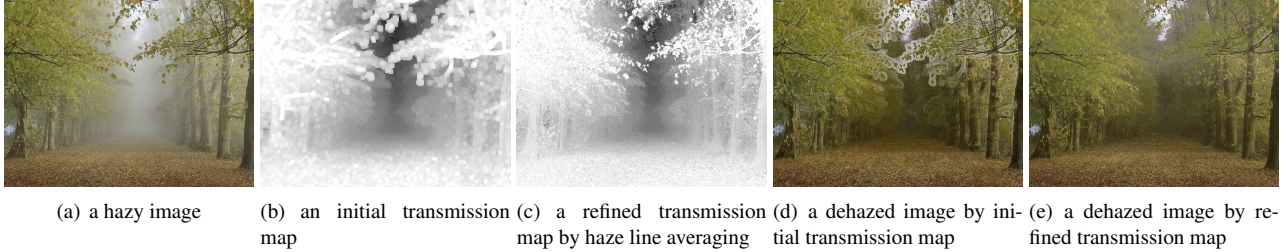


Figure 2. Comparison of initial and refined transmission maps as well as their corresponding dehazed images.

[22] is replaced by the Res2Net in [23] to well capture the multi-scale features at a granular level. Both spatial attention module and channel attention module are utilized in [22]. The modules can suppress the less useful features and only allow the propagation of more informative ones. Therefore, they effectively deal with the uneven distribution of haze. The discriminator is based on the PatchGAN in [24].

3.2.2 Loss Functions of Data-Driven Refinement

Besides the structure of the proposed GAN, loss functions also play an important role in the proposed GAN. Since both the atmospheric light A and transmission map $t(p)$ are refined by the GAN, the loss functions are defined by using the following restored image I :

$$I(p) = \frac{Z(p) - A}{\max\{t(p), 0.1\}} + A. \quad (8)$$

The proposed loss functions are associated with the training datasets. Since it is difficult for synthesized images to faithfully represent the distribution of real-world hazy images, it could be arguable to train the GAN by only using synthetic hazy images [29]. Thus, the proposed GAN is trained by using 500 images from the MRFID dataset [19] and 500 images with heavy haze regenerated from the RESIDE dataset [40]. The RESIDE dataset is an image dehazing benchmark set, and ground-truth images are available in the RESIDE dataset. The MRFID dataset contains foggy and clean images of 200 outdoor scenes in different lighting conditions. For each scene, one clear image and four foggy images of different densities defined as slightly, moderately, highly, and extremely foggy, are manually selected from images taken from these scenes over the course of one calendar year. The generator is trained by such a hybrid strategy to fool the discriminator, while the discriminator is attempting to distinguish between the clean images and the restored images. As such, the proposed GAN aligns the distribution of the restored images with that of the clean images.

Due to the different lighting conditions, the clean images are not the ground-truth ones even though they are taken

from the same scenes. The conventional loss functions include l_1 and l_2 loss functions are not applicable for the MRFID dataset. A new loss function is proposed by introducing an extreme channel. Let $\bar{I}_c(p)$ be defined as

$$\bar{I}_c(p) = \min\{I_c(p), 255 - I_c(p)\}, \quad (9)$$

and the extreme channel of the image I is defined as

$$\phi_\rho(I)(p) = \psi_\rho(\bar{I})(p). \quad (10)$$

The limitation of DCP on both the sky regions and high brightness objects can be avoided via the extreme channel.

Considering a pair of hazy image Z and clean image T which are captured from the same scene, the corresponding haze-free image of the hazy image is I . It can be known from the conventional imaging model [42] that

$$[T(p), I(p)] = [L_T(p), L_I(p)]R(p), \quad (11)$$

where $L_T(p)$ and $L_I(p)$ are the intensities of ambient light when the images T and I are captured. $R(p)$ is the ambient reflectance coefficient of surface, and it highly depends on the smoothness or texture of the surface.

Since both the $L_T(p)$ and $L_I(p)$ are constant in a small neighborhood, $\phi_\rho(I)(p)$ and $\phi_\rho(T)(p)$ are usually determined by the reflection $R(p)$. Thus, it can be easily derived that

$$\phi_\rho(I)(p) \approx \phi_\rho(T)(p) \approx 0. \quad (12)$$

The mean square error (MSE) between the extreme channels of hazy and clean images in the MRFID dataset [19] is shown in Figure 3. It can be observed that the MSE is usually decreased when the haze degree is reduced from extremely to slightly. The first loss function for the MRFID dataset is defined by using the extreme channels $\phi_\rho(I)$ and $\phi_\rho(T)$ as

$$L_e = \frac{1}{WH} \sum_p \|\phi_\rho(I)(p) - \phi_\rho(T)(p)\|_2^2, \quad (13)$$

where W and H are the width and height of the image I , respectively. The loss function L_e can guarantee that the haze is well removed in the restored image I .

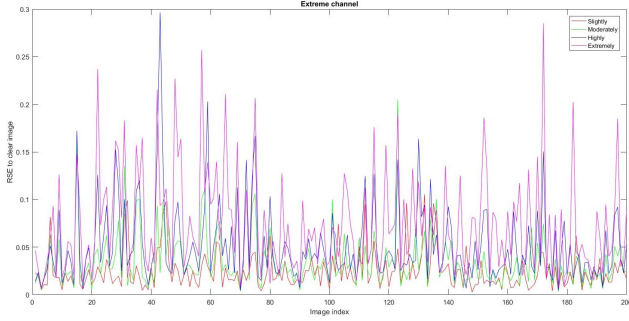


Figure 3. MSE between the extreme channels of hazy and clean images in the dataset [19].

The second loss function for the MRFID dataset is defined by using the gradients of the restored image I as

$$L_t = \frac{1}{WH} \sum_{p,c} (|\nabla_h I_c(p)| + |\nabla_v I_c(p)|), \quad (14)$$

where ∇_h and ∇_v represent the horizontal and vertical gradients, respectively. The loss function L_t can guarantee that the morphological artifacts are well reduced from the restored image I .

The third adversarial loss function for the MRFID dataset is defined by using the restored image I and clean image T as

$$L_{adv} = \log(D(T)) + \log(1 - D(I)), \quad (15)$$

where the PatchGAN in [24] is adopted as the discriminator D . The discriminator effectively models the image I as a Markov random field by assuming that pixels separated by more than a patch diameter are independent. The resultant loss can be understood as one type of texture loss. The loss function L_{adv} can guarantee that the textures and reflections of the images I and T are almost the same.

The overall loss function for the images in the MRFID dataset is defined as

$$L_{d,1} = w_{adv} L_{adv} + w_e L_e + L_t, \quad (16)$$

where w_{adv} and w_e are two constants, and their values are respectively selected as 20 and 10 if not specified in this paper. Experimental results in the section 4.2 show that the loss function L_t and the patch-based loss functions L_e and L_{adv} tend to smoothen the restored image.

The loss functions for the images in the RESIDE dataset are different from those image in the MRFID dataset. Since the ground-truth images are available in the RESIDE dataset, the conventional l_1 loss function and the feature-wise loss function via the fine-tuned VGG network for material recognition in [43] and the color distortion function in

[44] can be applied to define the loss functions for the corresponding restored images [30]. For simplicity, only the l_1 loss function is selected. The loss function for the images in the RESIDE dataset is defined as

$$L_{d,2} = \frac{1}{WH} \sum_p |I(p) - T(p)|, \quad (17)$$

where the image T is the ground-truth image.

The atmospheric light A and transmission map $t(p)$ in the equation (7) are refined by minimizing the following overall loss function in each batch:

$$L_d = w_R L_{d,2} + L_{d,1}, \quad (18)$$

where w_R is a constant, and its value is selected as 100 if not specified. The first and second terms are analogous to the data-fidelity and regularization terms of the optimization problems in [26, 37], respectively.

Our implementation is on top of a PyTorch framework with 4 NVIDIA GP100 GPUs. Both mirroring and randomly cropped $128 * 128$ patches from each input are employed to augment training data. The DNNs in Figure 1 are trained using the proposed loss functions and an Adam optimizer with the batch size as 16. The learning rate is initially set to 10^{-5} , then decreased using a cosine annealing schedule. The proposed algorithm is summarized as in the algorithm 1.

Algorithm 1: Model-based single image deep dehazing

- Step 1. Initialize the atmospheric light A_0 from the hazy image Z using the method in [21].
 - Step 2. Initialize the transmission map t_0 by using the DDAP as in the equation (3).
 - Step 3. Reduce the morphological artifacts of t_0 via the nonlocal haze line averaging (7).
 - Step 4. Refine the atmospheric light and transmission map using the GAN in Figure 1.
 - Step 5. Restore the haze free image I via the equation (8).
-

It can be easily verified by the images in Figure 2 that the dynamic range of the restored image is higher than that of the hazy image [5, 6]. Both the global contrast and the local contrast of the restored image are larger than those of the haze image. The restored image usually looks darker than the hazy image, and it can be brightened by using an existing single image brightening algorithm.

4. Experimental Results

Extensive experimental results on synthetic and real-world hazy images are provided in this section to validate

the proposed model-based deep learning framework with emphasis on illustrating how the model-based method and the data-driven method *compensate* each other in the proposed neural augmentation.

4.1. Datasets

The MRFID in [19] contains hazy and clean images of 200 outdoor scenes in different lighting conditions. The proposed GAN is trained by using the hazy and clean images of 125 outdoor scenes from the MRFID dataset with the corresponding 500 hazy images as well as 500 images with heavy haze generated using ground-truth images from the RESIDE dataset [40]. Depth is estimated by using the algorithm in [45]. The scattering coefficients of 100 images are randomly generated in $[1.2, 2.0]$ and those of the others are randomly selected in $[2.5, 3.0]$. The A_c 's are randomly generated in $[0.625, 1.0]$ for the color channel c independently. The hazy images of the 25 outdoor scenes from the MRFID dataset with the corresponding 100 hazy images are selected as the validation set. All these hazy images are randomly selected from the two datasets. The test images comprise 500 outdoor hazy images in the synthetic objective testing set (SOTS) [40], and 79 real-world hazy images in [10] which include 31 images are from the RESIDE [40], and the 19 images from [7] and the Internet.

4.2. Comparison of Different Training Strategies

Besides the proposed training strategy, two alternative training strategies are to: 1) use the 500 synthetic heavy haze images from the RESIDE dataset only with the l_1 loss function; and 2) use the 500 real-world hazy images from the MRFID dataset only with the three unsupervised loss functions in the equation (16). The former is a CNN based refinement while the latter is a GAN based refinement. Their network structures are the same as those in Figure 1. As shown in Figure 4, the trees look a little blurry in the red box by the CNN based refinement. Although the GAN based refinement is trained with real-world hazy images, all the loss functions in the equation (16) tend to over-smooth the restored image. Subsequently, the restored image is even blurrier as shown in Figure 4. The average DHQI values of the 100 hazy images in the validation dataset from the MRFID [19] are shown in Table 1. Clearly, the proposed framework can obtain a higher average DHQI value than the two alternative strategies.

Table 1. Average DHQI values of 100 hazy images in the validation dataset for different training strategies \uparrow .

CNN based	GAN based	Neural augmented	Data-driven
53.72	55.09	55.13	47.21

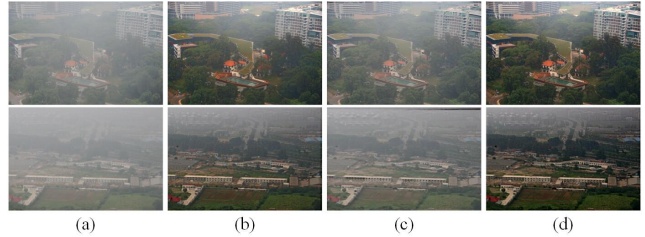


Figure 4. Comparison of different training strategies. From left to right, hazy images, de-hazed images by (b) CNN based strategy, (c) GAN based strategy, and (d) the proposed one.

4.3. Comparison with the Data-Driven Method

In order to verify the contribution of initial A and t from the model-based approach in the proposed neural augmentation de-hazing algorithm, the A and t are learnt directly by the same DNNs in Figure 1 without utilizing the initial values from the model-driven method. The average DHQI values of the 100 hazy images in the validation dataset from the MRFID [19] in different epochs are shown in Figure 5. The proposed framework converges faster and obtains higher DHQI values than the data-driven method. This is because that the residual information is sparser and it is more convenient to be learnt. The DHQI values of the finally de-hazed images by both the methods are shown in Table 1. Clearly, the proposed framework can obtain a higher average DHQI value than the data-driven method.

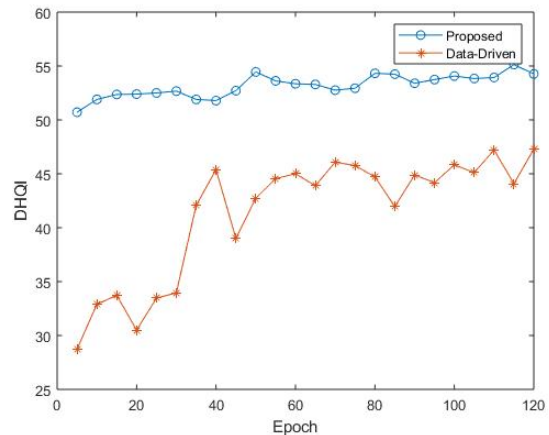


Figure 5. Comparisons of DHQI values between the data-driven method and the proposed neural augmentation in different training epochs.

4.4. Comparison of Different Dehazing Algorithms

The proposed dehazing algorithm is compared with seven state-of-the-art dehazing algorithms including RefinedNet [31], FFA-Net [14], PSD [20], DCP [35], HLP [9], MSBDN [15], and FD-GAN [39]. Among them, the algorithms HLP [9] and DCP [35] are model-based algorithms,

Table 2. Average PSNR and SSIM values of 500 outdoor hazy images in the SOTS for different algorithms \uparrow .

	FD-GAN [39]	RefineDNet [31]	FFA-Net [14]	PSD [20]	DCP [35]	HLP [9]	MSBDN [15]	Ours
PSNR	20.78	20.80	32.13	15.15	17.49	18.06	30.25	21.58
SSIM	0.863	0.898	0.979	0.735	0.855	0.849	0.944	0.874

Table 3. Average DHQI values of 79 real-world outdoor hazy images for different algorithms \uparrow .

	FD-GAN [39]	RefineDNet [31]	FFA-Net [14]	PSD [20]	DCP [35]	HLP [9]	MSBDN [15]	Ours
DHQI	51.00	57.57	55.33	50.60	51.92	52.75	54.32	59.86

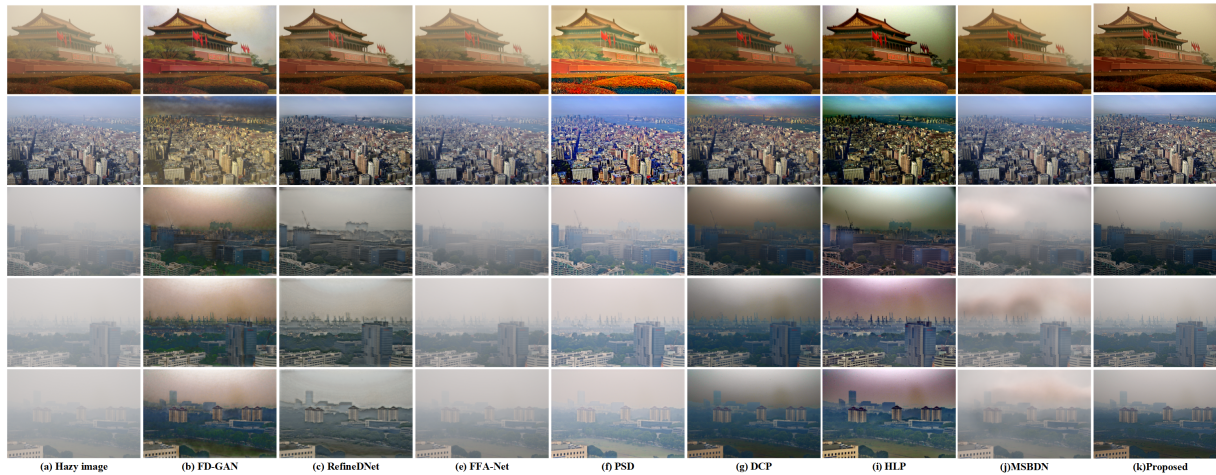


Figure 6. Comparison of different haze removal algorithms. From left to right, hazy images, dehazed images by FD-GAN [39], RefineDNet [31], FFA-Net [14], PSD [20], DCP [35], HLP [9], MSBDN [15], and ours, respectively.

the proposed algorithm and the RefineDNet [31] are combination of model-based and data-driven approaches, while the others are data-driven algorithms. The size of the input images must be dividable by 16 for the MSBDN [15]. Therefore, the sizes of the input images are resized for the MSBDN [15], and the restored images are resized back to the original ones. The sizes of several images exceed the GPU memory when using the FD-GAN [39], their sizes are reduced to half of the original ones, and the dehazed images are resized back to their original sizes.

The PSNR and SSIM are first adopted to compare the proposed algorithm with those in [31], [14], [20], [35], [9], [15], and [39] by using 500 synthetic outdoor hazy images in the SOTS [40]. The average PSNR values of the eight algorithms are given in Table 2. The FFA-Net [14] and MSBDN [15] are two CNN based dehazing algorithms, and they are optimized to provide high PSNR and SSIM values on the SOTS dataset. Both the proposed algorithm and the algorithm in [31] indeed outperform the model-based algorithms in [9] and [35].

The quality index DHQI in [41] is then adopted to compare the proposed algorithm with those in [31], [14], [20], [35], [9], [15], and [39] by using the 79 real-world hazy images in [10]. The average DHQI values of the 79 real-world outdoor hazy images are given in Table 3. Clearly, the proposed algorithm and the algorithm in [31] outperform others

from the DHQI point of view.

Finally, all these dehazing algorithms are compared subjectively as in Figure 6. Readers are invited to view to electronic version of figures and zoom in them so as to better appreciate differences among all images. Although the FFA-Net [14] and MSBDN [15] achieve high PSNR and SSIM value, their dehazed results are a little blurry and they are not photo-realistic. In addition, the haze is not reduced well if it is heavy. The DCP [35], HLP [9], RefineDNet [31], FD-GAN [39], and the proposed algorithm can be applied to generate photo realistic images. There are visible morphological artifacts in the restored images by the RefineDNet [31] and FD-GAN [39]. The DCP [35] and HLP [9] restore more vivid and sharper images at the expense of amplified noise in sky regions.

5. Conclusion Remarks and Discussion

A new single image dehazing algorithm is introduced by using model-based deep learning frameworks. Both transmission map and atmospheric light are obtained by a neural augmentation which consists of model-based estimation and data-driven refinement. They are then applied to restore a haze-free image. Experimental results validate that the proposed algorithm removes haze well from the synthetic and real-world hazy images. The proposed neural augmentation reduces the number of training data significantly.

References

- [1] Srinivasa G. Narasimhan and Shree K. Nayar. Contrast restoration of weather degraded images. *IEEE Trans. On Pattern Analysis and Machine Learning*, 25(6): 713-724, 2003. 1
- [2] Kshitiz Garg and Shree K. Nayar. Detection and removal of rain from videos. In *IEEE/CVF Conference on Computer Vision and Pattern Recognition*, 2004. 1
- [3] Codruta Orniana Ancuti and Cosmin Ancuti. Single image dehazing by multi-scale fusion. *IEEE Trans. on Image Processing*, 22(8): 3271–3282, 2013. 1
- [4] Kaiming He, Jian Sun, and Xiao Ou Tang. Single image haze removal using dark channel prior. *IEEE Trans. On Pattern Analysis and Machine Learning*, 33(12): 2341-2353, 2011. 1, 2, 3
- [5] Jinghong Zheng, Zhengguo Li, Zijian Zhu, Shiqian Wu, and Susanto Rahardja. Hybrid patching for a sequence of differently exposed images with moving objects. *IEEE Trans. on Image Processing*, 22(12): 5190-5201, 2013. 1, 2, 6
- [6] Fei Kou, Zhe Wei, Weihai Chen, Xinming Wu, Changyun Wen, and Zhengguo Li. Intelligent detail enhancement for exposure fusion. *IEEE Trans. on Multimedia*, 20(2): 484–495, 2018. 1, 6
- [7] Raanan Fattal. Dehazing using color-lines. *ACM Trans. on Graphics*, 34(1): article 13, 2014. 1, 2, 7
- [8] Qingsong Zhu, Jiaming Mai, and Ling Shao. A fast single image haze removal algorithm using color attenuation prior. *IEEE Trans. on Image Processing*, 24(11): 3522-3533, 2015. 1, 2, 3
- [9] Dana Berman, Tali Treibitz, and Shai Avidan. Non-local Image Dehazing. In *IEEE/CVF Conference on Computer Vision and Pattern Recognition (CVPR)*, 1674-1682, 2016. 1, 2, 3, 4, 7, 8
- [10] Zhengguo Li, Haiyan Shu, and Chaobing Zheng. Multi-scale single image dehazing Using Laplacian and Gaussian pyramids. *IEEE Trans. on Image Processing*, 30(12): 9270-9279, 2021. 1, 2, 3, 4, 7, 8
- [11] Wenqi Ren, Si Liu, Hua Zhang, Jinshan Pan, Xiaochun Cao, and Ming-Hsuan Yang. Single image dehazing via multi-scale convolutional neural networks. In *European Conference on Computer Vision*, pp 154-169, Sept. 2016. 1, 3
- [12] Bolun Cai, Xiangmin Xu, Kui Jia, Chunmei Qing, and Dacheng Tao. DehazeNet: an end-to-end system for single image haze removal. *IEEE Trans. on Image Processing*, 25(11): 5187-5198, 2016. 1, 3
- [13] Boyi Li, Xiulian Peng, Zhangyang Wang, Jizheng Xu, and Dan Feng. AOD-Net: all-in-one dehazing network. In *IEEE/CVF International Conference on Computer Vision*, pp. 4780-4788, Oct. 2017. 1
- [14] Xu Qin, Zhilin Wang, Yuanchao Bai, Xiaodong Xie, and Huizhu Jia. FFA-Net: Feature fusion attention network for single image dehazing. In *AAAI Conference on Artificial Intelligence*, 11908-11915, 2020. 1, 2, 3, 7, 8
- [15] Hang Dong, Jinshan Pan, Lei Xiang, Zhe Hu, Xinyi Zhang, Fei Wang, and Ming-Hsuan Yang. Multi-scale boosted dehazing network with dense feature fusion. In *IEEE/CVF Conference on Computer Vision and Pattern Recognition (CVPR)*, 2020. 1, 2, 3, 7, 8
- [16] Yanyun Qu, Yizi Chen, Jingying Huang, and Yuan Xie. Enhanced Pix2pix dehazing network. In *IEEE/CVF Conference on Computer Vision and Pattern Recognition (CVPR)*, 8152-8160, Jun. 2019. 1, 3
- [17] H. Koschmieder, Theorie der horizontalen sichtweite. In *Proc. Beitrage Phys. Freien Atmos.*, 33-53, 1924. 1, 2, 3
- [18] Alona Golts, Daniel Freedman, and Michael Elad, Un-supervised single image dehazing using dark channel prior loss. *IEEE Trans. on Image Processing*, 29: 2692 - 2701, 2019. 1, 3
- [19] Wei Liu, Fei Zhou, Tao Lu, Jiang Duan, and Guoping Qiu. Image defogging quality assessment: real-world database and method. *IEEE Trans. on Image Processing*, 30: 1762–190, 2021. 1, 2, 3, 5, 6, 7
- [20] Zeyuan Chen, Yangchao Wang, Yang Yang, and Dong Liu. PSD: principled synthetic-to-real dehazing guided by physical priors. In *IEEE/CVF Conference on Computer Vision and Pattern Recognition*, 2021. 1, 7, 8
- [21] Jin-Hwan Kim, Won-Dong Jang, Jae-Young Sim, and Chang-Su Kim. Optimized contrast enhancement for real-time image and video dehazing. *Journal of Visual Communication and Image Representation*, 24(3): 410-425, Apr. 2013. 1, 4, 6
- [22] Syed Waqas Zamir, Aditya Arora, Salman Khan, Munawar Hayat, Fahad Shahbaz Khan, Ming-Hsuan Yang, and Ling Shao. CycleISP: real image restoration via improved data synthesis. In *IEEE/CVF Conference on Computer Vision and Pattern Recognition*, 2020. 1, 3, 4, 5
- [23] Shang-Hua Gao, Ming-Ming Cheng, Kai Zhao, Xin-Yu Zhang, Ming-Hsuan Yang, and Philip Torr. Res2Net: A New Multi-scale Backbone Architecture.

- IEEE Trans. on Pattern Analysis and Machine Intelligence, 43(2), 652-662, 2021. 1, 5
- [24] Phillip Isola, Jun-Yan Zhu, Tinghui Zhou, and Alexei A. Efros. Image-to-image translation with conditional adversarial networks. In *IEEE/CVF Conference on Computer Vision and Pattern Recognition*: 1125-1134, 2017. 1, 3, 5, 6
- [25] Nir Shlezinger, Jay Whang, Yonina C. Eldar, and Alexandros G. Dimakis. Model-based deep learning. arXiv: 2012.08405v2 [eess.SP] 27 Jun 2021. 1, 2, 3
- [26] Zhengguo Li and Jinghong Zheng. Single image de-hazing using globally guided image filtering. *IEEE Trans. on Image Processing*, 27(1): 442-450, 2018. 2, 3, 6
- [27] He Zhang and Vishal M. Patel. Densely connected pyramid dehazing network. In *IEEE/CVF Conference on Computer Vision and Pattern Recognition*, pp. 3194-3203, 2018. 3
- [28] Yuanjie Shao, Lerenhan Li, Wenqi Ren, Changxin Gao, and Nong Sang. Domain adaptation for image dehazing. In *IEEE/CVF Conference on Computer Vision and Pattern Recognition*, pp. 2808-2817, 2020. 3
- [29] Xitong Yang, Zheng Xu, and Jiebo Luo. Towards perceptual image dehazing by physics-based disentanglement and adversarial training. In *Proceedings of the AAAI Conference on Artificial Intelligence*, 2018. 3, 5
- [30] Lerenhan Li, Yunlong Dong, Wenqi Ren, Jinshan Pan, Changxin Gao, Nong Sang, and Ming-Hsuan Yang. Semi-supervised image dehazing. *IEEE Trans. on Image Processing*, 29:2766-2779, 2020. 3, 6
- [31] Shiyu Zhao, Lin Zhang, Ying Shen, and Yicong Zhou. RefineDNet: A weakly supervised refinement framework for single image dehazing. *IEEE Trans. on Image Processing*, 30: 3391-3404, 2021. 2, 3, 7, 8
- [32] Chaobing Zheng, Zhengguo Li, Yi Yang, and Shiqian Wu. Single image brightening via multi-scale exposure fusion with hybrid learning. *IEEE Trans. on Circuits and Systems for Video Technology*, 31(4): 1425-1435, 2021. 3
- [33] Kurt Hornik, Maxwell Stinchcombe, Halbert White, et al.. Multilayer feedforward networks are universal approximators. *Neural Networks*, 2(5):359-366, 1989. 1, 4
- [34] Michael T. Orchard and Charles A. Bouman. Color quantization of images. *IEEE Trans. on Signal Processing*, 39(12): 2677-2690, 1991. 2
- [35] Kaiming He, Jian Sun, and Xiao Ou Tang. Guided image filtering. *IEEE Trans. on Pattern Analysis and Machine Intelligence*, 35(6): 1397-1409, 2013. 2, 3, 4, 7, 8
- [36] Zhengguo Li, Jinghong Zheng, Zijian Zhu, Yei Wei, and Shiqian Wu. Weighted guided image filtering. *IEEE Trans. on Image Processing*, 24(1): 120-129, 2015. 2, 4
- [37] Zeev Farbman, Raanan Fattal, Dani Lischinski, and Richard Szeliski. Edge-preserving decompositions for multi-scale tone and detail manipulation. *ACM Trans. on Graphics*, 27(3): 249-256, 2008. 2, 6
- [38] Ian J. Goodfellow, Jean Pouget-Abadie, Mehdi Mirza, Bing Xu, David Warde-Farley, Sherjil Ozair, Aaron Courville, and Yoshua Bengio. Generative adversarial nets. In *NIPS 2014*, Canada, Dec. 2014. 1, 2, 4
- [39] Yu Dong, Yihao Liu, He Zhang, Shifen Chen, and Yu Qiao. FD-GAN: Generative adversarial networks with fusiondiscriminator for single image dehazing. In *Proceedings of the AAAI Conference on Artificial Intelligence*, 34: 10728-10736, 2020. 2, 3, 7, 8
- [40] Boyi Li, Wenqi Ren, Dengpan Fu, Dacheng Tao, Dan Feng, Wenjun Zeng, and Zhangyang Wang. Benchmarking single-image dehazing and beyond. *IEEE Trans. on Image Processing* 28(1):492-505, 2018. 2, 3, 5, 7, 8
- [41] Xionguo Min, Guangtao Zhai, Ke Gu, Xiaokang Yang, and Xinpeng Guan. Objective quality evaluation of dehazed images. *IEEE Trans. on Intelligent Transportation Systems*, 20(8): 2879-2892, 2019. 2, 8
- [42] Rafael C. Gonzalez and Richard E. Woods. *Digital Image Processing*. Englewood Cliffs, NJ, USA: Prentice-Hall, 2002. 5
- [43] Sean Bell, Paul Upchurch, Noah Snavely, and Kavita Bala. Material recognition in the wild with the materials in context database. In *IEEE/CVF Conference on Computer Vision and Pattern Recognition*, 2015. 6
- [44] Yuki Endo, Yoshihiro Kanamori, and Jun Mitani. Deep reverse tone mapping. *ACM Trans. Graphics*, 36(6): 1-10, 2017. 6
- [45] Zhengqi Li and Noah Snavely. Megadepth: Learning single-view depth prediction from internet photos. In *IEEE/CVF Conference on Computer Vision and Pattern Recognition*, 2041-2050, 2018. 7